Publishing Excellence Inspiring Progress
ARISTON PUBLICATIONS
Quantum Advances
ISSN: 3143-0724 www.aristonpubs.com/journal/quantum-advances https://doi.org/10.69626/qa.2025.0004

RESEARCH ARTICLE

Mixed effects of laser dressing and electric fields on linear optical properties and Raman scattering of ZnO/MgZnO quantum wells

S. Uran-Parra*

ABSTRACT: The combined effects of a non-resonant intense laser field (ILF) and an external electric field on the electronic structure and optical response of an asymmetric ZnO/$Mg_xZn_{1-x}O$ quantum well within the effective mass approximation and the Kramers-Henneberger formalism is investigated theoretically and numerically. The interplay between laser-induced dressing of the confinement potential and the electric-field-induced asymmetry leads to significant modifications of the subband structure, including energy shifts, wave function redistribution, and polarity-dependent localization. As a consequence, the linear optical absorption exhibits pronounced redshifts and variations in peak amplitude, reflecting changes in both transition energies and dipole coupling. The Raman differential cross section reveals the coexistence of resonant peak-like features and step-like structures associated with threshold activation of scattering channels, whose spectral positions and intensities are strongly modulated by the dressing parameter. In particular, a non-monotonic dependence on the laser parameter is observed, with distinct behaviors depending on the electric field polarity. The Raman gain further highlights this interplay, showing a dramatic enhancement of several orders of magnitude under resonant conditions, together with a strong sensitivity to small variations of the dressing parameter due to the competition between resonance tuning and wave function delocalization. These results demonstrate that the combined action of intense laser fields and external electric fields provides a highly flexible mechanism for controlling both linear and nonlinear optical properties in polar quantum well systems, with potential applications in tunable optoelectronic and photonic devices.

Keywords: Quantum Wells; Intense Laser Fields; Stark Effect; Optical Absorption; Raman Scattering; Nonlinear Optical Response.

Received: 25 September 2025; Revised: 03 November 2025; Accepted: 11 November 2025; Published Online: 05 December 2025

1. INTRODUCTION

Semiconductor quantum wells (QWs) represent a fundamental platform for investigating quantum confinement and its influence on the optoelectronic response of low-dimensional systems. Among the wide variety of semiconductor materials, ZnO-based heterostructures have been garnering attention due to their wide direct bandgap ($\sim$ 3.37 eV), large exciton binding energy ($\sim$60 meV), and significant optical response in the UV region [1–5]. These features make ZnO-based systems suitable for optoelectronic and photonic applications at room temperature. In addition, their compatibility with different growth techniques and nanostructured morphologies has enabled the fabrication of high-quality low-dimensional systems with improved optical properties [6–10].

Particularly, $Mg_xZn_{1-x}O$ alloys has demonstrated additional tunability in the continuous engineering of bandgap and confinement potential through compositional control [11–15]. In wurtzite phase ZnO/MgZnO QWs, the absence of the inversion symmetry produces strong spontaneous and

Grupo de Materia Condensada-UdeA, Instituto de Física, Facultad de Ciencias Exactas y Naturales, Universidad de Antioquia UdeA, Cl 70 No. 52-21, Medellín, Colombia.

*Author to whom correspondence should be addressed: salomon.uran@udea.edu.co (S. Uran-Parra)

© Ariston Publications 2025. All rights reserved.

piezoelectric polarization fields, giving rise to built-in electric fields along the growth direction. These fields tilt the conduction confinement potential and breaks the possible spatial symmetry of the system, modifying significantly electronic distribution probabilities and intersubband transitions. From this, ZnO/MgZnO QWs exhibit highly tunable optical properties, making them ideal candidates for the study of field-driven effects in quantum-confined systems [16–19].

Apart from structural and intrinsic effects, external perturbations are a powerful mechanism for controlling the energy of electron states. In particular, the use of non-resonant intense laser fields (ILFs) has been an effective approach to the dynamic tailoring of the confinement potential. Within the Kramers-Henneberger framework, the ILF induces an average oscillatory displacement of the electronic distributions, leading to laser-dressed potentials that differ significantly from the initial confinement profile. This laser-induced effect does not alter real electronic transitions but instead reshapes the effective potential profile, indirectly changing subband energies, wave functions, and transition matrix elements [20–23]. From this, ILFs are capable of ultrafast control of electronic and optical properties in semiconductor nanostructures.

An additional versatile mechanism to control optoelectronic features of confined states in semiconductor systems involves the application of an external electric field, generating the so called quantum-confined Stark effect (QCSE). The influence of an applied field leads to a tilted confinement potential, giving direct spatial separation of electron and hole wave functions along the growth direction. From this, the overlap and Coulomb interaction are reduced, resulting in a redshift of transition energies and a suppression of oscillator strengths. The literature has extensively confirmed this behavior in semiconductor heterostructures and even in more recent and novel material platforms, where strong electric fields can induce pronounced modifications of excitonic and intersubband transitions [24, 25].

From this, since the electric field alters the selection rules for optical transitions, it enables tunable control of absorption and emission processes. Furthermore, the distortion induced on the electronic states affects both confined and continuous spectra, which is especially relevant for photoionization and nonlinear optical responses [26]. Recently, for example, this modulation mechanism has been exploited in nanostructured systems for optoelectronic applications, where QCSE-based electroabsorption provides an efficient route for dynamic control of optical emission [27]. In polar systems such as ZnO/MgZnO QWs, an external electric field interacts with internal polarization fields, giving rise to a complex interplay that determines carrier localization, tunneling phenomena, and the overall optical responses of the system.

Optical absorption processes often provide direct insight into the quantized energy spectrum of semiconductor heterostructures. Particularly, the photoionization cross sections and intersubband absorption spectra are highly sensitive to confinement geometry, external fields, and Coulomb interactions. Variations in structural parameters such as well width and barrier thickness directly modify energy levels and wave functions, shifting the absorption peaks and changing their intensity. The external perturbations, such as electric and laser fields, further enhance this tunability by modifying the effective potential and matrix elements. In wide-bandgap semiconductors such as ZnO, the strong excitonic effects and electron-impurity interactions can influence the absorption spectra, producing pronounced resonances and sensitivity to external control [17–19].

In parallel, Raman scattering has become a powerful tool for probing vibrational, electronic, and many-body effects in semiconductor heterostructures. In opposition to linear absorption, Raman processes involve inelastic light scattering, which provides access to transitions between vibrational and electronic states through nonlinear interactions. The Raman differential cross section (DCS) and Raman gain are especially sensitive to the electronic structure, confinement potential, and other interaction mechanisms in the system [28, 29]. However, Raman scattering is typically a inherently weak phenomenon, which limits its direct applicability in low-dimensional systems.

Nevertheless, recent advances in improved Raman techniques, such as surface-enhanced Raman scattering, show that local electromagnetic fields can dramatically amplify Raman emissions, enabling sensitivity even for single-molecule measurements [30, 31]. This enhancement arises primarily from localized surface plasmon resonances, which increase both the incident and scattered radiation fields. In addition, nonlinear Raman processes, including coherent Raman scattering, benefit even more from these local field enhancements, as their intensities scale with higher powers of the radiation field.

Considering this state of the art, this work investigates the combined influence of an external electric field and a non-resonant intense laser field on the electronic and optical properties of a $ZnO/Mg_xZn_{1-x}O$ asymmetric quantum well. Particular attention is devoted to the interplay between these external perturbations and the intrinsic polarization fields, and their impact on intersubband transitions, optical absorption, and Raman scattering

 © Ariston Publications 2025. All rights reserved.

processes. By analyzing the evolution of energy levels, dipole matrix elements, absorption spectra, Raman differential cross section, and Raman gain, we provide a comprehensive understanding of how external fields can be used to tailor the optical response of polar quantum well systems.

The remainder of this paper is structured as follows. In Section 2, we describe the theoretical framework and the physical model of the ZnO/$Mg_xZn_{1-x}O$ quantum well, including the formulation of the laser-dressed potential under an external electric field and the corresponding Schrödinger equation. In Section 3, we present and analyze the numerical results, focusing on the evolution of the confinement potential, electronic energy levels, optical absorption, Raman differential cross section, and Raman gain as functions of the dressing parameter and electric field. Finally, in Section 4, we summarize the main findings and provide concluding remarks.

2. THEORY

2.1 Electronic confinement in ZnO/$Mg_xZn_{1-x}O$ quantum wells under polarization fields and external bias

We consider an asymmetric ZnO/$Mg_xZn_{1-x}O$ single quantum well (QW) grown along the z-direction. The structure is formed by a ZnO well region of width $L_w = 20$ nm confined by two $Mg_xZn_{1-x}O$ barriers of width $L_b = 15$ nm, and the Mg concentration is taken as $x = 0.2$. As mentioned in the introduction, ZnO-based heterostructures exhibit strong spontaneous and piezoelectric polarization effects. As a result, polarization charges accumulate at the interfaces, generating built-in electrostatic fields that strongly tilt the conduction band profile. Within the effective mass approximation, the electron distribution is described by a confinement potential $V(z)$ along the growth direction. The total confinement potential considered includes three contributions: the conduction band offset between ZnO and $Mg_xZn_{1-x}O$, the internal polarization-induced electric fields, and the external electric field F. Therefore, the potential takes the piecewise form [32]:

$$V(z) = \begin{cases} eF_b(z - L_b) + eFz + \Delta E_c, & 0 < z < L_b, \\ eF_w(z - L_b) + eFz, & L_b < z < L_b + L_w, \\ eF_b(z - L_b - L_w) + & \\ eF_wL_w + eFz + \Delta E_c, & L_b + L_w < z < L. \end{cases} \tag{1}$$

where $L = L_w + 2L_b$ is the total heterostructure length, ΔE_c is the conduction band discontinuity, and F_w and F_b are the internal electric fields in the well and barrier regions, respectively. The conduction band offset is assumed to follow an usual 75% band offset ratio [33, 34]:

$$\Delta E_c = 0.75 \left(E_{g,\mathrm{Mg}_x\mathrm{Zn}_{1-x}\mathrm{O}} - E_{g,\mathrm{ZnO}} \right) \tag{2}$$

This parameter determines the confinement strength of the electronic states. A larger ΔE_c yields stronger confinement and generally pushes the excited states upward while enhancing wave function localization inside the ZnO well. Since the barrier band gap depends on the Mg concentration x, the composition provides an efficient way to tune the confinement potential and, consequently, the optical properties of the system.

The built-in fields are obtained from the electrostatic continuity conditions across the interfaces and are written as [32]:

$$F_w = \frac{2L_bP_{\mathrm{tot}}}{2\varepsilon_bL_b + \varepsilon_wL_w}, \qquad F_b = -F_w\frac{L_w}{2L_b} \tag{3}$$

where P_{tot} is the total polarization, while ε_w and ε_b are the dielectric constants of the well and barrier materials, respectively. Table 1 displays all the numerical values and concentration dependencies on the heterostructure parameters used in the calculations.

2.2 Laser dressing and Schrödinger equation

When the heterostructure is irradiated by a non-resonant intense laser field (ILF), the electronic confinement is modified through the interaction of the carriers with the oscillatory electromagnetic field. For sufficiently high frequency and under non-resonant conditions, the laser field does not induce direct intersubband transitions in the usual sense; instead, it renormalizes the effective confinement profile experienced by the electron. This regime can be described within a semiclassical framework using the Kramers--Henneberger transformation, which transfers the explicit time dependence of the field from the Hamiltonian to the confinement potential. Under this approach, the dressed electronic states are obtained from the one-dimensional Schrödinger equation in the envelope-function formalism:

$$-\frac{\hbar^2}{2}\frac{d}{dz}\left(\frac{1}{m^*(z)}\frac{d\psi_j(z,\alpha_0)}{dz}\right) + \tilde{V}(z,\alpha_0)\psi_j(z,\alpha_0) = E_j(\alpha_0)\psi_j(z,\alpha_0) \tag{4}$$

© Ariston Publications 2025. All rights reserved.

where $m^*(z)$ is the position dependent effective mass, $\psi_j(z,\alpha_0)$ is the envelope wave function of the jth confined state, and $E_j(\alpha_0)$ is the corresponding eigenenergy. α_0 is the laser-dressing parameter, which measures the amplitude of the laser-induced oscillatory displacement of the electron. The dressed potential is obtained by averaging the translated confinement potential over one time period of the field [35]:

$$\tilde{V}(z,\alpha_0) = \frac{1}{T}\int_0^T V[z+\alpha_0\sin(\omega_0 t)]\,dt, \tag{5}$$

where ω_0 is the angular frequency of the laser field and $T = 2\pi/\omega_0$ is its period. The validity of the effective mass approximation under this action relies on the fact that the relevant transitions occur near the conduction-band minimum, where the dispersion remains nearly parabolic. In ZnO-based quantum wells, non-parabolicity becomes relevant only at substantially higher carrier energies. Since the present work focuses on low-lying intersubband transitions, the effective mass formalism remains physically adequate.

2.3 Linear optical absorption and thermal occupation of the subbands

The absorption of an incident photon promotes an electron from an initial confined state ψ_i to a final state ψ_j, provided that the photon energy matches the intersubband transition energy. In the present model, the optical response is treated within the density-matrix formalism combined with perturbation theory, which yield a linear absorption coefficient written as [36].:

$$\alpha_{ij}^{(1)}(\omega) = \hbar\omega\,\frac{\Xi_{ij}}{\tau_{in}}\,\frac{|M_{ij}|^2}{(E_j-E_i-\hbar\omega)^2+(\hbar/\tau_{in})^2}, \tag{6}$$

where ω is the angular frequency of the incident photon, τ_{in} is the intersubband relaxation time, and

$$\Xi_{ij} = \sqrt{\frac{\mu_0}{\varepsilon_0\varepsilon}}\,\sigma_{ij}, \qquad M_{ij} = \langle\psi_i|z|\psi_j\rangle. \tag{7}$$

Here, M_{ij} is the transition matrix element, which measures the strength of the optical coupling between the two states, while σ_{ij} is the difference in volumetric carrier density between the subbands involved in the transition. Equation (6) has the usual Lorentzian structure: the absorption reaches its maximum close to the resonance condition $\hbar\omega = E_j - E_i$, and its amplitude is controlled by both the dipole overlap and the occupation difference. Consequently, any external parameter capable of modifying the subband energies or wave function distribution as the electric field, Mg concentration, or laser dressing will alter both the position and intensity of the absorption peaks.

Because the carrier population is temperature dependent, thermal effects must be incorporated explicitly. The population of the ith confined state is determined through the Fermi-Dirac distribution:

$$n_i = \frac{m_w^*}{\pi\hbar^2}\int_{E_i}^{\infty}\frac{dE}{1+\exp\left(\frac{E-E_f}{k_BT}\right)}, \tag{8}$$

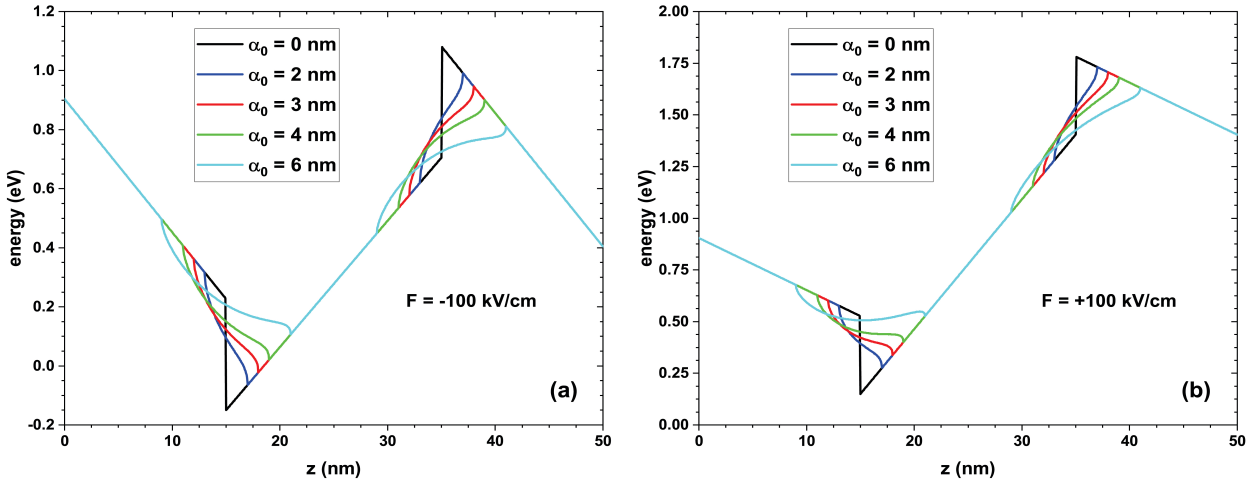

Fig. 1. Evolution of the confinement potential profile as a function of the dressing parameter α_0 in a ZnO/$Mg_xZn_{1-x}O$ quantum well with dimensions $L_w = 20$ nm and $L_b = 15$ nm. In (a), the structure is subjected to an external electric field $F = -100$ kV/cm, while in (b) the field is reversed ($F = +100$ kV/cm). The progressive smoothing of the potential with increasing α_0 reflects the laser-induced renormalization of the confinement.

© Ariston Publications 2025. All rights reserved.

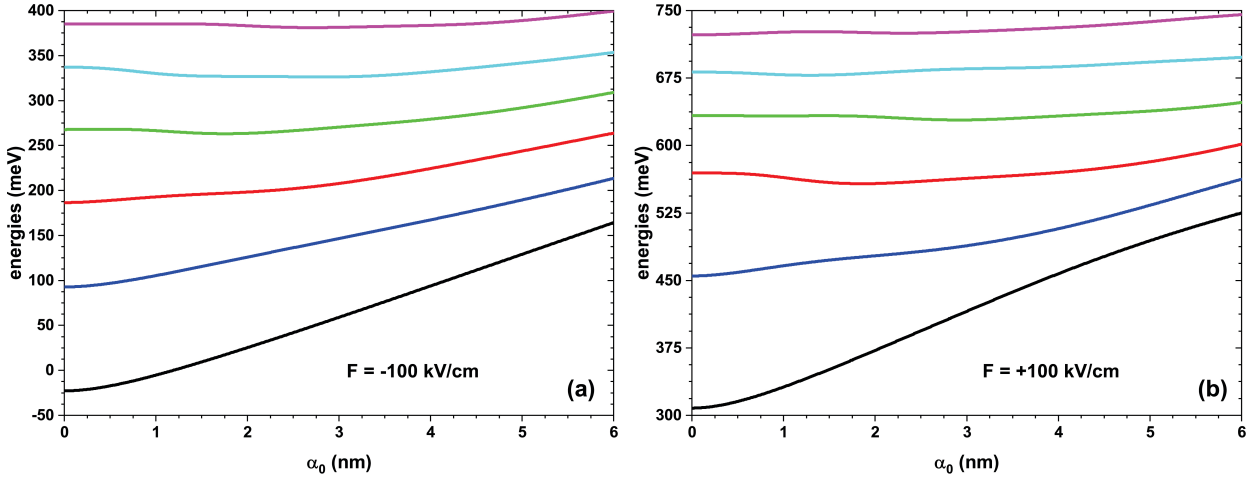

Fig. 2. Dependence of the first six confined electronic energy levels on the dressing parameter α_0 in a ZnO/$Mg_xZn_{1-x}O$ quantum well with $L_w = 20$ nm and $L_b = 15$ nm. Panel (a) corresponds to $F = -100$ kV/cm, while (b) corresponds to $F = +100$ kV/cm. The monotonic increase of the energy levels with α_0 evidences the effective weakening of the confinement potential.

where m_w^* is the effective mass in the well material, E_f is the Fermi level, and T is the temperature. This expression shows that the occupation of each subband is not fixed but depends on the relative position of the state energy with respect to the Fermi level. As temperature increases, the electronic distribution broadens, and the ground state population is progressively redistributed toward higher subbands. From this expression is possible to calculate the respective Fermi level E_f using the total superficial carrier density relation given by $n_d = \sum_{i=0}^{N} n_i$. Then, the population difference entering the absorption coefficient is then given by [36]:

$$\sigma_{ij} = \frac{m^* k_B T}{\pi \hbar^2 L} \ln\left[\frac{1+\exp\left(\frac{E_f - E_i}{k_B T}\right)}{1+\exp\left(\frac{E_f - E_j}{k_B T}\right)}\right]. \tag{9}$$

.

2.4 Raman differential cross section

Raman scattering in semiconductor nanostructures is a second order optical process in which the system absorbs incident radiation and re-emits radiation at a different frequency through an intermediate virtual or real electronic state.

$$\frac{d^2\sigma}{d\Omega\, d\nu_s} = \vartheta(\nu_L, \nu_s)\, W(\nu_s, \hat{u}_s), \tag{10}$$

where σ is the scattering cross section, Ω is the solid angle, ν_L and ν_s are the frequencies of the incident and scattered radiation, respectively, and $\hat{u}_s$ is the polarization unit vector of the emitted field. The prefactor $\vartheta(\nu_L, \nu_s)$ is

$$\vartheta(\nu_L, \nu_s) = \frac{\nu_s^2 n(\nu_s)}{8\pi^3 c^4 n(\nu_L)}, \tag{11}$$

with $n(\nu_L)$ and $n(\nu_s)$ the refractive indices at the incident and scattered frequencies and c the speed of light. The quantity $W(\nu_s, \hat{u}_s)$ is the Raman transition rate.

In intersubband Raman processes, the spectral response is highly sensitive to the confined-level structure, the electron-photon coupling, and the broadening of the intermediate and final states. This makes Raman spectroscopy a valuable probe of quantum confinement and carrier dynamics. The fundamental quantity describing the Raman process is the differential cross section (DCS), expressed as [35]:

For the present three-level configuration, the Raman process is modeled as an absorption step $\psi_0 \to \psi_2$ followed by an emission step $\psi_2 \to \psi_1$. The transition rate is written as [35]:

$$W(\nu_s, \hat{u}_s) = \frac{2}{\hbar} \times \frac{|T_{021}|^2}{(E_s + E_1 - E_2)^2 + \Gamma_a^2} \times \frac{\Gamma_f}{(E_L - E_s + E_0 - E_1)^2 + \Gamma_f^2} \tag{12}$$

and $\Gamma_a = \Gamma_f = 5$ meV [28] are the broadenings of the intermediate and final states, respectively. These phenomenological parameters account for

© Ariston Publications 2025. All rights reserved.

Table 1. Material and physical parameters employed in the modeling of the ZnO/$Mg_xZn_{1-x}O$ quantum well system.

Quantity	Symbol (Units)	Expression / Value
Temperature	T (K)	300
Well internal electric field	F_w (MV/cm)	0.52
Barrier internal electric field	F_b (MV/cm)	-0.35
Conduction band offset	ΔE_c (meV)	376.5
Effective mass [32]	m^* (m_0)	$0.23 + 0.05x$
Dielectric constant [32]	ε (ε_0)	$8.1 + 1.5x$
Total polarization [32]	P_{tot} (C/m^2)	$0.032x$
Intrasubband relaxation time [32]	τ_{in} (ps)	0.24
Laser field intensity [32]	I_L (W m^{-2})	1×10^{10}
Bandgap energy [37]	E_g (eV)	$3.37 + 2.51x$
Surface carrier density [38]	n_d (cm^{-2})	8.5×10^{11}

finite lifetimes and dephasing processes produced by electron-phonon interaction and additional damping mechanisms. Their inclusion is essential because real physical transitions are not infinitely sharp. In fact, the Raman peaks acquire a finite linewidth that determines the spectral selectivity and peak amplitude.

Since the system is one-dimensional along the growth direction, the polarization vectors of the incident and emitted fields can be taken along z, i.e. $\hat{u}_L = \hat{u}_s = (1, 0, 0)$ in the notation of the original model, and the photon-electron interaction operator becomes [35]:

$$H_k = -\frac{ie\hbar}{m_0}\sqrt{\frac{2\pi\hbar^3}{V\nu_k}}\frac{\partial}{\partial z}, \tag{13}$$

where m_0 is the free-electron mass, ν_k is the radiation frequency, and $V = \frac{2}{\sigma_{01}}$ is the QW volume. The matrix element associated with H_k is directly linked to the velocity operator between confined states. Therefore, Raman scattering is not controlled only by the energy-level spacings but also by the derivative structure of the wave functions.

2.5 Nonlinear susceptibility and Raman gain

Beyond the DCS, another central quantity is the Raman gain, which measures the amplification of the emitted coherent radiation through stimulated Raman scattering. In semiconductor quantum wells, Raman gain is especially useful because it combines the effects of quantum confinement, resonance tuning, and carrier population into a single observable quantity. The gain coefficient is obtained from the third-order nonlinear susceptibility $\chi^{(3)}$, which for the present intersubband system is written as [35]:

$$\chi^{(3)}(E_s, E_L) = -i\frac{\sigma_{01}|M_{02}|^2|M_{12}|^2}{\varepsilon_0\left[(E_2 - E_0 - E_L)^2 + \Gamma^2\right]\Gamma}. \tag{14}$$

In this expression, σ_{01} is the population difference between the initial and final states participating in the Raman process, while M_{02} and M_{12} are the transition matrix elements associated with the absorption and emission channels. The denominator contains the detuning with respect to the intermediate state and the linewidth parameter $\Gamma = \hbar/\tau_{in}$. Equation (14) shows that the nonlinear response is enhanced under near-resonant conditions and when the wave function overlaps are large. The Raman gain coefficient is then expressed as

$$G_R(E_s, E_L) = \frac{\omega_s}{nc}\,\text{Im}\left[\chi^{(3)}(E_s, E_L)\right]|E|^2, \tag{15}$$

where $n = \sqrt{\varepsilon_v\mu}$ is the refractive index, ω_s is the angular frequency of the scattered radiation, and E is the pump-field amplitude. Since the gain is proportional to the imaginary part of the nonlinear susceptibility, it becomes maximum when the combined conditions of strong dipole coupling, favorable occupation difference, and small detuning are simultaneously satisfied. The pump intensity $I_L = 1 \times 10^{10}$ W m^{-2} [32] is related to the field amplitude through:

$$I_L = \frac{1}{2}nc\varepsilon_0|E|^2. \tag{16}$$

In the present framework, the incident energy E_L spans the range required to promote the electron from the ground state toward a virtual intermediate configuration before emission. Introducing the detuning parameter $\delta = 5$ meV, one may write [39]:

$$\delta = E_2 - E_2' = E_2 - E_0 - E_L, \tag{17}$$

so that the pump energy is selected according to the resonance condition shifted by δ. This

© Ariston Publications 2025. All rights reserved.

representation is useful because it makes explicit that the Raman response is governed by the energetic proximity between the laser photon and the relevant intersubband excitation pathway. In this sense, using the detuning δ, one can expect that an incident energy $E_L = \max\{E_2 - E_0\} - \delta$ yields a maximum in gain intensity.

3. RESULTS AND DISCUSSIONS

Figure 1 shows the evolution of the confinement potential as a function of the laser-dressing parameter a_0 under opposite polarities of the external electric field. A clear asymmetry is observed between panels (a) and (b), which originates from the direction of the applied electric field and its interplay with the laser-induced renormalization. In Figure 1 (a), corresponding to $F = -100$ kV/cm, the potential is tilted such that the left and right barrier profile becomes almost parallel, enabling more concentrated densities in the well region. For $a_0 = 0$, the profile exhibits a strongly asymmetric triangular-like shape due to the combined effect of band offset and internal polarization fields. As a_0 increases, the influence of the intense laser field becomes evident through a progressive smoothing of the potential profile, particularly around the minimum region. This smoothing reduces the sharpness of the confinement and slightly elevates the bottom of the well, indicating a weakening of the effective confinement strength. At larger a_0 values, the potential becomes flatter in the central region, facilitating a redistribution of the electronic density toward both sides of the left interface.

In contrast, Figure 1 (b) corresponds to the reversed field ($F = +100$ kV/cm), where the tilting of the potential is inverted: the left barrier is lower than the right side, since it becomes steeper. Although the same laser-dressing mechanism is present, its effect is now superimposed on a different asymmetric configuration. As a_0 increases, the smoothing of the potential is again observed, but its impact is more pronounced near the shifted minimum, which is displaced toward the left-hand side of the structure. The combination of field polarity and laser dressing leads to a distinct reshaping of the confinement, with a reduction of the effective barrier height and a modification of the spatial extent of the well. The comparison between Figure 1 (a) and 1 (b) highlights that the parameter a_0 does not act independently, but rather modulates a field-dependent potential landscape. While increasing a_0 consistently induces a smoothing and partial flattening of the confinement in both cases, the final shape of the potential is strongly conditioned by the direction of the external electric field. This interplay between field polarity and laser-induced renormalization is crucial, as it determines the localization properties of the electronic states and sets the basis for the different trends observed in the energy spectrum and optical responses discussed in subsequent figures. Figure 2 displays the evolution of the first six confined electronic energy levels as a function of the laser-dressing parameter a_0 under opposite external electric field polarities. While a general increase of all energy levels with a_0 is observed in both panels, important differences arise between Figure 2 (a) and 2(b) due to the asymmetric modification of the confinement potential discussed in Figure 1. The potential profile in Figure 2 (a), corresponding to $F = -100$ kV/cm, is tilted and modified such that the minimum is shifted toward the central part of the well, where the confinement is relatively sharper. As a_0 increases, the laser-induced smoothing weakens this confinement, leading to a progressive increase in all energy levels. This effect is particularly pronounced for the lower states, which are more strongly localized near the potential minimum and therefore more sensitive to changes in the curvature of the well. As a result, the ground and first excited states exhibit a steeper dependence on a_0, while higher-energy states show a more moderate variation due to their already extended spatial character.

In opposition, Figure 2 (b), corresponding to $F = +100$ kV/cm, exhibits a different behavior arising from the inversion of the potential asymmetry. In this case, the minimum is shifted toward the left-hand side, where the confinement is effectively softer. Consequently, even at $a_0 = 0$, the electronic states are more delocalized compared to Figure 2 (a). As the laser-dressing parameter increases, the additional smoothing of the potential produces a more gradual increase in the energy levels, particularly for the lowest states. The weaker initial confinement reduces the sensitivity of these states to the laser-induced renormalization, resulting in smaller slopes compared to those observed in Figure 2 (a). Figure 3 presents the linear optical absorption coefficient as a function of the incident photon energy for different values of the dressing parameter a_0 under opposite electric field orientations. Starting from Figure 3 (a) ($F = -100$ kV/cm), the absorption resonances systematically shift toward lower photon energies as a_0 increases, indicating a reduction in the effective confinement energy. At the same time, the peaks remain relatively sharp and well-defined, with only moderate changes in their amplitude. This behavior reflects a regime where the electronic states, although affected by the laser -

© Ariston Publications 2025. All rights reserved.

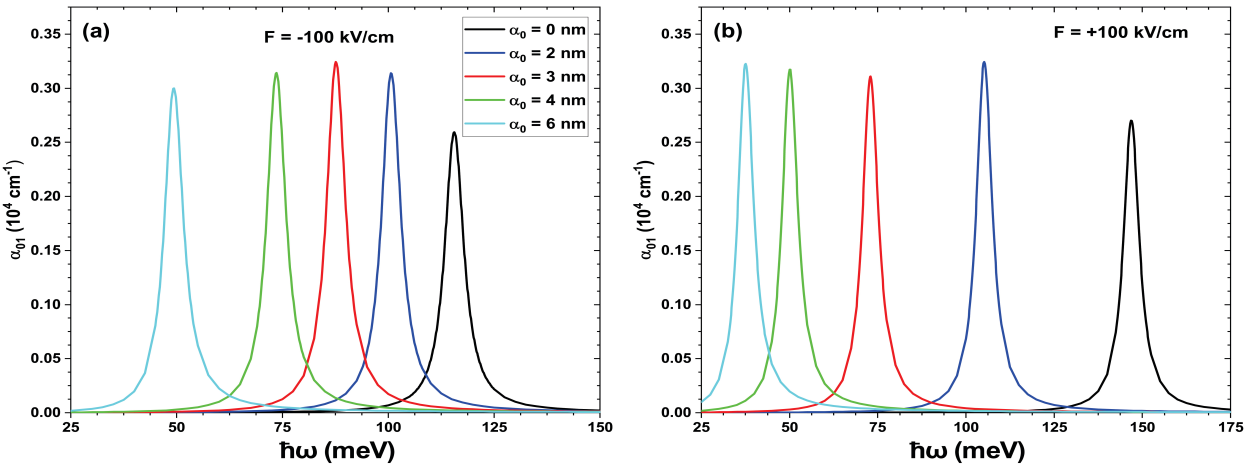

Fig. 3. Linear optical absorption coefficient $\alpha^{(1)}$ as a function of the incident photon energy $\hbar\omega$ for different values of the dressing parameter α_0 in a ZnO/$Mg_xZn_{1-x}O$ quantum well ($L_w = 20$ nm, $L_b = 15$ nm). In (a), the system is under an electric field $F = -100$ kV/cm, while in (b) the field is $F = +100$ kV/cm. The shift and amplitude variation of the peaks are governed by the interplay between electric field asymmetry and laser-induced delocalization.

induced smoothing of the potential, remain sufficiently localized. Consequently, the transition energies are strongly renormalized, but the overlap between initial and final states is not drastically altered.

A different scenario is observed in Figure 3 (b) for $F = +100$ kV/cm. Here, the absorption peaks also undergo a redshift with increasing a_0, but their evolution is accompanied by a more noticeable redistribution of spectral weight. In particular, the peaks become slightly broader and their amplitudes exhibit more pronounced variations compared to panel (a). This indicates that the electronic states are more sensitive to the laser dressing under this field polarity, which is consistent with the softer confinement profile discussed previously. The enhanced delocalization of the wave functions leads to a stronger modification of the dipole coupling, thereby affecting both the position and intensity of the optical transitions.

It is important to note that, although the system temperature is fixed at $T = 300$ K, variations in the volumetric carrier density do not play a significant role in the present analysis. This is because the electronic population is effectively governed by the thermal occupation factor, which strongly favors the ground state due to the relatively large intersubband energy separations in ZnO/$Mg_xZn_{1-x}O$ quantum wells. In particular, the Boltzmann factor $\exp[-(E_i - E_f)/k_BT]$ ensures that the occupation of excited states remains negligible under the considered conditions. As a consequence, the carrier distribution can be accurately approximated as entirely localized in the ground state, and transitions originating from higher-energy subbands are safely neglected. This justifies why the optical absorption is dominated by the transition between the ground and first excited states, while transitions involving the first and second excited states are suppressed by the lack of initial population. Furthermore, direct transitions from the ground to the second excited state are also negligible due to the vanishing (or extremely small) dipole matrix elements imposed by symmetry and selection rules. Therefore, the combined effect of thermal occupation and transition matrix elements supports the restriction of the analysis to the lowest intersubband transition. The behavior of the dipole matrix elements shown in Figure 4 manifest the direct influence of the external fields in the evolution of the transition strengths as a function of the dressing parameter a_0. In Figure 4 (a), corresponding to $F = -100$ kV/cm, the matrix element $|M_{12}|^2$ clearly dominates over the others and exhibits an abrupt increase with a_0, specially around $\alpha_0 = 2$nm, indicating an enhancement of the coupling between the first two excited confined states. In contrast, $|M_{01}|^2$ shows a little weaker dependence, steady increasing with α_0 in a smooth way, suggesting that the wave functions for this transition remain well localized with a gradually improvement in the spatial overlaping; $|M_{02}|^2$ remains negligible across the entire range, consistent with the expected selection rules and limited overlap between non-adjacent states.

A qualitative change is present in Figure 4, where the electric field is reversed ($F = +100$ kV/cm). In this case, the growth of $|M_{12}|^2$ with a_0 is significantly more pronounced, especially

 © Ariston Publications 2025. All rights reserved.

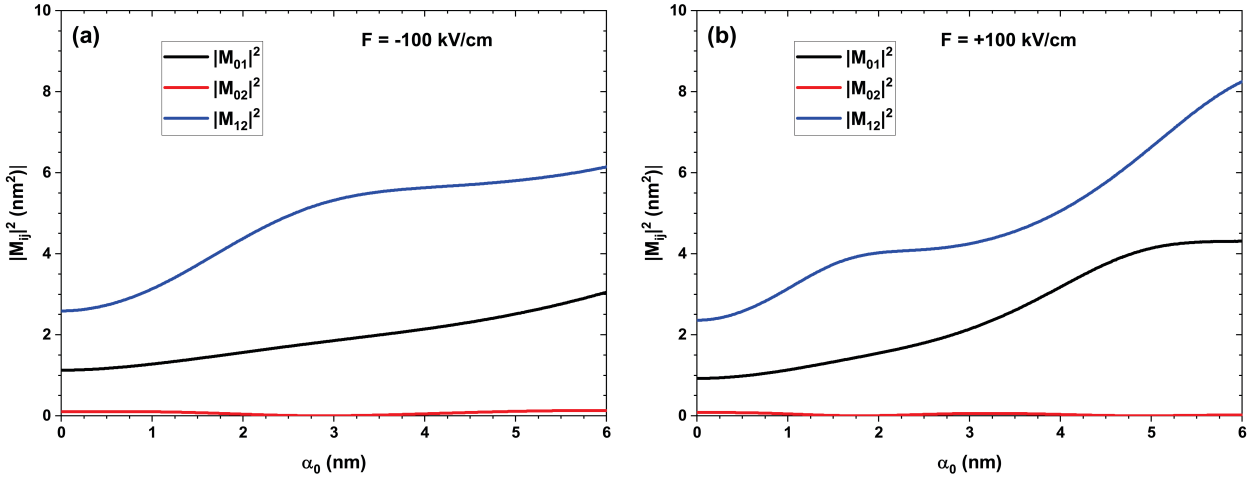

Fig. 4. Dipole matrix elements $|M_{ij}|^2$ for the first three confined states as a function of the dressing parameter α_0 in a ZnO/$Mg_xZn_{1-x}O$ quantum well ($L_w = 20$ nm, $L_b = 15$ nm). Panel (a) corresponds to $F = -100$ kV/cm, while (b) corresponds to $F = +100$ kV/cm. The dominant contribution from $|M_{12}|^2$ reflects enhanced overlap between adjacent states under laser dressing.

at larger values of the dressing parameter. This behavior reflects a stronger redistribution of the electronic wave functions, which enhances their spatial overlap beyond what is observed in panel (a). Additionally, the same can be said for $|M_{01}|^2$, since it exhibits a more visible increase compared to the negative-field case, indicating that the modified confinement allows for improved coupling between lower states. The overall enhancement of the dipole matrix elements under this field orientation is consistent with a more delocalized electronic structure, as previously inferred from the potential profile and energy spectrum. Lastly, the case for $|M_{02}|^2$ remains negligible, similar at the situation in panel (a). Figure 5 shows the Raman differential cross section (DCS) as a function of the scattered photon energy E_s under different excitation and field conditions. A key feature of these spectra is the coexistence of two distinct types of structures: well-defined resonant peaks and step-like discontinuities. These contributions arise from discrete intersubband transitions and from threshold-like access to intermediate states in the Raman scattering process. In the high incident energy regime (Figure 5 (a) and 5 (b), $E_L = 400$ meV), both features are clearly visible. The Lorentzian-like peaks shift with increasing a_0, reflecting the renormalization of the subband energies, while the step-like structures mark the activation of new scattering channels when intermediate states become resonant. The position of these steps therefore follows the evolution of the electronic structure under laser dressing.

A comparison between Figure 5 (a) ($F = +100$ kV/cm) and 5 (b) ($F = -100$ kV/cm) reveals that the balance between resonant and step-like contributions is strongly influenced by the field polarity. For $F = +100$ kV/cm, the spectra are smoother, dominated by broader resonances, whereas in comparison, for $F = -100$ kV/cm the peaks positions are more separated and its magnitude are lower for both peaks, indicating a more discrete activation of scattering channels due to stronger localization asymmetry. This asymmetry becomes even more evident when analyzing the dependence on the dressing parameter a_0. In the positive field configuration (Figure 5 (a) and 5 (c)), the DCS does not decrease monotonically with increasing a_0. Instead, a clear enhancement is observed at $a_0 = 3$ nm relative to $a_0 = 2$ nm, followed by a subsequent reduction at larger values of a_0. This behavior indicates that an intermediate level of laser dressing optimizes the overlap between initial, intermediate, and final states, leading to a transient increase in the Raman efficiency before delocalization effects dominate and suppress the signal.

In contrast, for the negative field configuration (Figure 5 (b) and 5 (d)), the dependence on a_0 exhibits the opposite trend: the DCS reaches a minimum around $a_0 = 3$ nm. In this case, the combined effect of the electric field and the laser-induced renormalization leads to a configuration where the coupling between states is reduced, likely due to an unfavorable spatial redistribution of the wave functions. As a_0 increases further, the DCS partially recovers, suggesting that the system moves away from this inefficient coupling regime. Under resonant excitation (Figure 5 (c) and 5 (d)), these trends are further amplified. In Figure 5 (c), the dominant peak remains strong and reflects the

© Ariston Publications 2025. All rights reserved.

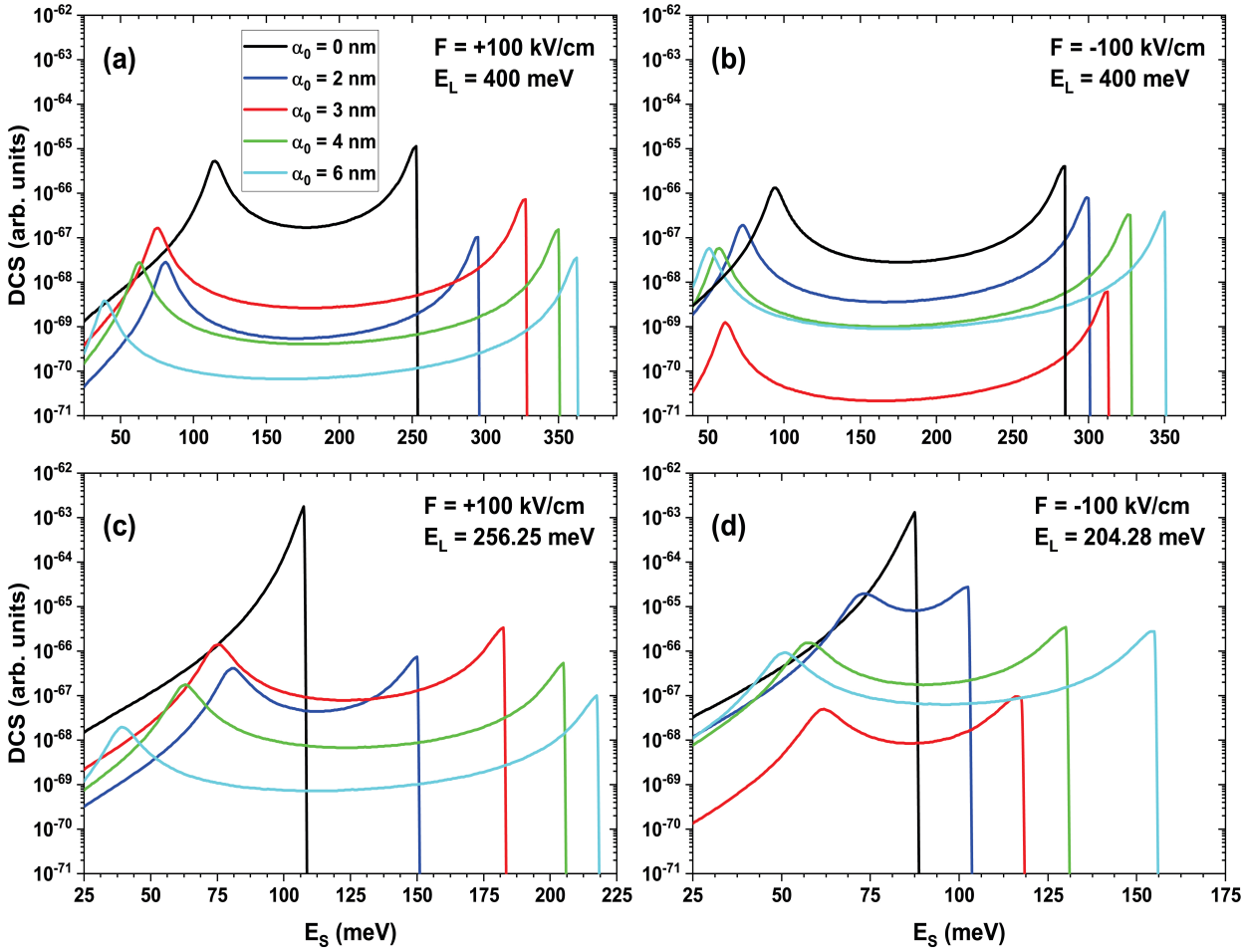

Fig. 5. Raman differential cross section (DCS) as a function of the scattered photon energy E_s for different values of the dressing parameter α_0. Panels (a) and (b) correspond to incident energy $E_L = 400$ meV with $F = +100$ kV/cm and $F = -100$ kV/cm, respectively, while (c) and (d) correspond to resonant conditions with $E_L = 256.25$ meV and $E_L = 204.28$ meV. The spectral features reflect the modification of intersubband transitions by the combined effects of the electric field and laser dressing.

optimal coupling at intermediate a_0, whereas in Figure 5 (d) the spectrum becomes more fragmented, with competing peaks and step-like features that evolve non-uniformly. The sensitivity of the resonant condition to both field polarity and laser dressing highlights the delicate balance governing the Raman process. Figure 6 presents the Raman gain as a function of the dressing parameter a_0 under different excitation energies and electric field orientations. A striking feature of these results is the drastic difference in magnitude between the off-resonant and resonant regimes. While the gain in Figure 6 (a) and 6 (b) ($E_L = 400$ meV) remains on the order of 10^{-2}-10^{-1} cm^{-1}, the resonant cases shown in Figure 6 (c) and 6 (d) reach values as high as 10^2 cm^{-1}, evidencing an enhancement of several orders of magnitude. This contrast reflects the dominant role of resonance in amplifying the nonlinear optical response. In the off-resonant regime (Figure 6 (a) and 6 (b)), the gain is relatively weak and exhibits a smooth but non-monotonic dependence on a_0. In both cases, the gain decreases rapidly from its maximum at $a_0 = 0$, reaching a minimum at intermediate values of the dressing parameter. The subsequent behavior depends on the electric field polarity: for $F = -100$ kV/cm (Figure 6 (a)), a partial recovery of the gain is observed at larger a_0, whereas for $F = +100$ kV/cm (Figure 6 (b))) the gain remains strongly suppressed over the entire range. This indicates that, in the absence of resonance, the laser-induced delocalization of the electronic states dominates the response, reducing the overlap between states and weakening the Raman process. A completely different behavior emerges under resonant excitation (Figure 6 (c) and 6 (d)), where the gain is dramatically enhanced and becomes highly sensitive to small variations of a_0. In both panels, the gain exhibits a sharp maximum at low values of the dressing parameter, corresponding to optimal alignment between the incident photon

 © Ariston Publications 2025. All rights reserved.

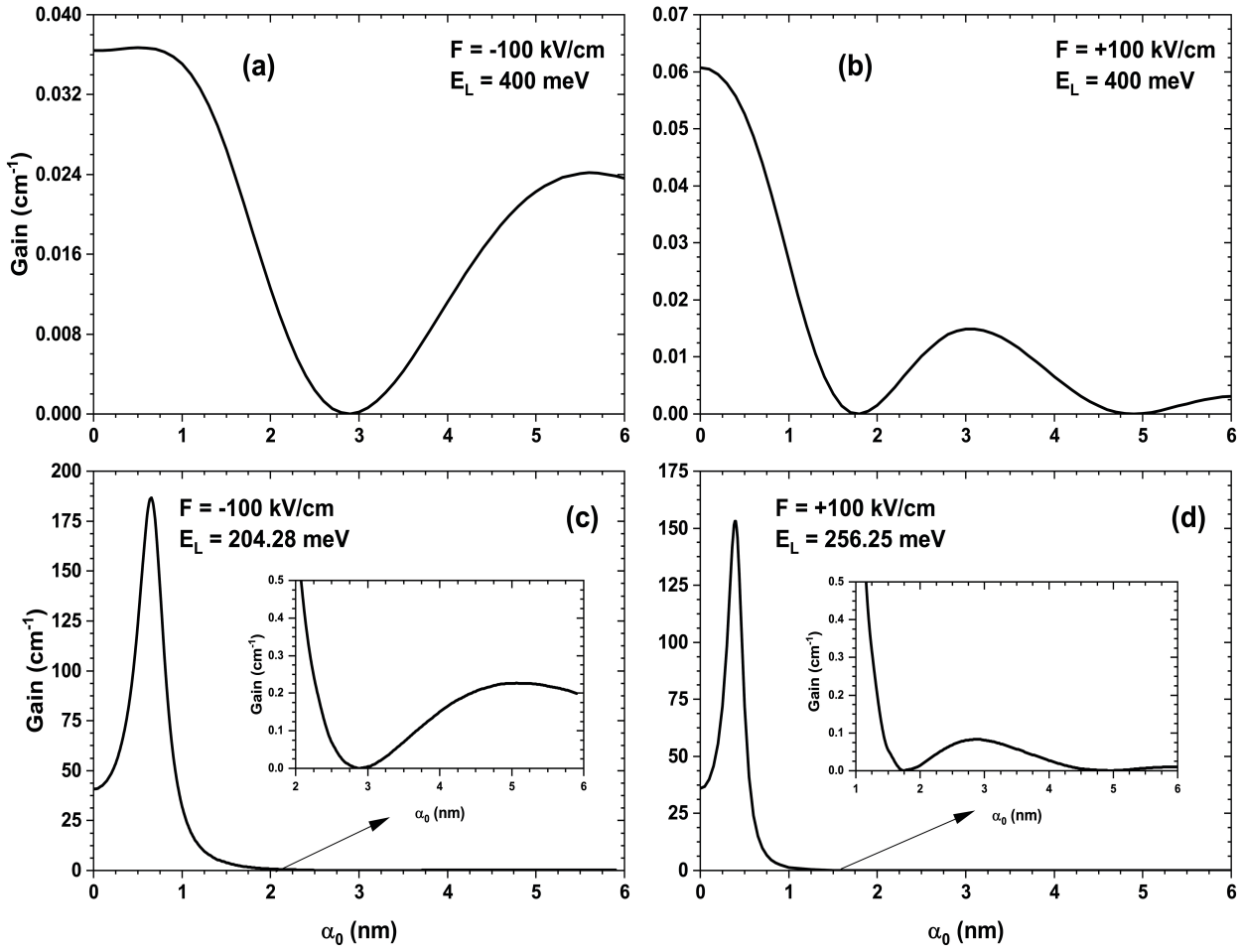

Fig. 6. Raman gain as a function of the dressing parameter α_0 in a ZnO/$Mg_xZn_{1-x}O$ quantum well. Panels (a) and (b) correspond to $E_L = 400$ meV under $F = -100$ kV/cm and $F = +100$ kV/cm, respectively, while (c) and (d) correspond to resonant excitation conditions. The reduction of gain with increasing α_0 highlights the suppression of nonlinear optical response due to wavefunction delocalization.

energy and intersubband transitions. However, this strong enhancement is rapidly quenched as a_0 increases, reflecting the fact that even slight modifications of the confinement potential are sufficient to detune the resonance condition. This leads to a steep reduction of the gain by several orders of magnitude over a relatively narrow range of a_0. The influence of the electric field polarity is particularly evident when comparing Figure 6 (c) and 6 (d). For $F = +100$ kV/cm (Figure 6 (d))), the gain peak is extremely sharp and localized, indicating a highly selective resonance condition that is quickly lost as a_0 increases. In contrast, for $F = -100$ kV/cm (Figure 6 (c)), the peak is slightly broader and followed by a smoother decay, suggesting that the resonance is less abruptly disrupted due to a more gradual redistribution of the electronic states. This behavior is consistent with the different localization characteristics imposed by the electric field, which affect how sensitively the system responds to laser-induced renormalization.

Finally, the inset panels reveal that the gain does not vanish monotonically at large a_0, but instead exhibits shallow minima followed by slight recoveries, in agreement with the non-monotonic trends and minima in $\alpha_0 = 3$ nm observed in the DCS (Figure 5). This indicates that the Raman gain is governed by competing mechanisms: laser-induced delocalization reduces the transition probability, while simultaneous shifts in the energy spectrum can partially restore favorable resonance conditions. Overall, the results highlight that the Raman gain is controlled by a delicate balance between resonance enhancement and wave function overlap. The dramatic difference in magnitude between off-resonant and resonant regimes, combined with the strong sensitivity to both a_0 and electric field polarity, demonstrates the potential for achieving highly tunable nonlinear optical amplification in ZnO/MgZnO quantum well systems.

© Ariston Publications 2025. All rights reserved.

4. CONCLUSION

The present work deployed a theoretical and numerical study of the electronic structure and optical properties of an asymmetric $ZnO/Mg_xZn_{1-x}O$ quantum well under the combined influence of a non-resonant intense laser field and an external electric field. The results show that the quantum-confined Stark effect induces a tilting of the confinement potential, leading to energy blueshifts, wave function separation, and reduced transition strengths, while the laser field modifies the effective potential through dressing effects, enabling redistribution and partial recovery of electronic localization. The interplay between these two mechanisms gives rise to a highly tunable behavior in both linear and nonlinear optical responses, as evidenced by significant shifts and variations in the linear optical absorption, Raman differential cross section, and Raman gain. In particular, the competing effects of field-induced carrier separation and laser-induced confinement renormalization allow for precise control of transition energies and intensities. These findings highlight the potential of combined external perturbations as an effective strategy for engineering the optical response of polar quantum well systems and support their applicability in the design of tunable optoelectronic and photonic devices.

DECLARATIONS

Ethical Approval

We affirm that this manuscript is an original work, has not been previously published, and is not currently under consideration for publication in any other journal or conference proceedings. All authors have reviewed and approved the manuscript, and the order of authorship has been mutually agreed upon.

Funding

There are no funding

Availability of data and material

All of the data obtained or analyzed during this study is included in the report that was submitted.

Conflicts of Interest

The authors declare that they have no financial or personal interests that could have influenced the research and findings presented in this paper. The authors alone are responsible for the content and writing of this article.

Authors' contributions

All authors contributed equally in the preparation of this manuscript.

REFERENCES

[1] Tang, Y. M. and Ji, X. H. and Qu, Y., **2025**. Dual peaks of optical absorption in MgZnO/AlGaN core-shell nanowires. *Micro and Nanostructures*, 207, p.208284. https://doi.org/10.1016/j.micrna.2025.208284.

[2] Meenakshi and Kumar, A. and Rinki and Dutta, M. and Srivastava, S. K. and Sehgal, G. and Singh, S. and Gupta, G. and Fix, T. and Pathi, P., **2025**. Tunable physical and electrical characteristics of AZO/p-Si heterostructures developed using super-cycle approach of ALD. *Journal of Materials Science: Materials in Electronics*, 36, p.1481. https://doi.org/10.1007/s10854-025-15511-6.

[3] Karuppiah, V. and Kader, K. R. A., **2025**. Simulation of Quantum Dot Nanocable Rectifiers Integrated with MgZnO/ZnO-based High Electron Mobility Transistors. *Semiconductors*, 59, p.616-631. https://doi.org/10.1134/S1063782624602954.

[4] Karuppiah, V. and Kader, K. R. A., **2026**. Exploring the Potential of MgZnO/ZnO High Electron Mobility Transistors in High-Frequency and Low-Noise Applications. *Semiconductors*, 60, p.163-176. https://doi.org/10.1134/S1063782625603620.

[5] Saha, R. and Mahapatra, S. and Dalal, A. and Mondal, A. and Chakrabarti, S., **2025**. Investigation of dual-wavelength selective self-powered photo response of ZnO/Si heterojunction with insertion of thin TiO2 layer. *Applied Physics A*, 131, p.11. https://doi.org/10.1007/s00339-024-08155-6.

[6] Gupta, G. and Verma, S. and Nagarajan, R. and Rath, S., **2021**. Microstructural and

 © Ariston Publications 2025. All rights reserved.

bandgap investigations of wurtzite-phase ZnMgO nanopowders synthesized by ball-milling. *Physica B*, 604, p.412735. https://doi.org/10.1016/j.physb.2020.412735.

[7] Verma, Y. K. and Dheep, R. and Adhikari, M. S., **2024**. Analysis of electrical performance of MgZnO/ZnO high electron mobility transistor. *Journal of the Korean Physical Society*, 84, p.299-306. https://doi.org/10.1007/s40042-023-00996-3.

[8] Zhao, W. and Zhou, D. and Sui, J. and Tong, Y. and Wang, X. and Zhu, L., **2025**. Demonstration of ferroelectricity in Zn1-xMgxO thin films over a wide Mg concentration range. *Journal of Materials Science: Materials in Electronics*, 36, p.1100. https://doi.org/10.1007/s10854-025-15197-w.

[9] Vinothkumar, K. and Rahuman, A. K., **2025**. Modeling and Simulation of Nanometer Al-Doped Dual Channel Double Material Gate MgZnO/ZnO HEMT for High-Frequency Applications. *Transactions on Electrical and Electronic Materials*, 26, p.00667. https://doi.org/10.1007/s42341-025-00667-z.

[10] Guo, Q. and Zhang, B. and Sun, B. and Qi, Y., **2024**. Cu, Ni and Ag ions assisted preparation of nonpolar preferential oriented ZnO films with controlled morphology and optical properties. *Journal of Alloys and Compounds*, 971, p.172683. https://doi.org/10.1016/j.jallcom.2023.172683.

[11] Hao, Y. and Wang, C. and Guo, L. and Sun, Y. and Jin, M. and Xu, L. and Huang, Y. and Zong, Y. and Xu, X. and Zeng, J., **2025**. Fabrication and Electrical Characterization of MgZnO/ZTO Thin-Film Transistors. *Nanomaterials*, 15, p.1809. https://doi.org/10.3390/nano15231809.

[12] Gu, Z. and Tang, H. and Zhou, X., **2025**. Interband multilevel transitions in ZnO/MgZnO asymmetric double quantum wells. *Chemical Physics*, 598, p.112820. https://doi.org/10.1016/j.chemphys.2025.112820.

[13] Bappy, N. F. and Subramani, S., **2025**. A comprehensive review on Mg-doped ZnO thin film and nanostructure: Properties and applications. *Materials Science and Engineering B*, 318, p.118251. https://doi.org/10.1016/j.mseb.2025.118251.

[14] Zhong, Q. and Wu, C. and Yu, X. and Yu, X. and Li, Z. and Qiao, Q. and Zhou, Y. and Cao, Y., **2023**. Mg content regulating built-in electric field for self-powered ZnO/MgxZn1-xO Schottky UV photodetector. *Optical Materials*, 146, p.114572. https://doi.org/10.1016/j.optmat.2023.114572.

[15] Wang, J. X. and Qu, Y. and Ban, S. L., **2023**. Ternary mixed crystal effects on optical phonons in wurtzite ZnO quantum wells with asymmetric MgZnO barriers. *Micro and Nanostructures*, 184, p.207685. https://doi.org/10.1016/j.micrna.2023.207685.

[16] Yarar, Z. and Alyörük, M. D. and Çekil, H. C. and Özdemir, B. and Özdemir, M., **2024**. Mobility Characteristics of ZnMgO/ZnO Heterostructures with Screening Effects. *Physics of the Solid State*, 66, p.91-98. https://doi.org/10.1134/S1063783423600061.

[17] Gu, Z. and Li, Z. and Liang, J. and Tian, H. and Jiang, H. and Li, G. and Tang, H., **2022**. Linear and nonlinear optical properties in wurtzite MgZnO/ZnO double quantum wells: Roles of external electric and magnetic fields. *Micro and Nanostructures*, 169, p.207341. https://doi.org/10.1016/j.micrna.2022.207341.

[18] Andrzejewski, J. and Pietrzyk, M. A. and Jarosz, D. and Kozanecki, A., **2021**. Optical Measurements and Theoretical Modelling of Excitons in Double ZnO/ZnMgO Quantum Wells in an Internal Electric Field. *Materials*, 14, p.7222. https://doi.org/10.3390/ma14237222.

[19] Hassani, F. and Haghighatzadeh, A. and Aezami, A., **2026**. High-intensity electric field orientation-dependent optoelectronic response in a laser-affected GaAs0.75Sb0.25/GaAs Morse quantum well. *Physica E*, 179, p.116498. https://doi.org/10.1016/j.physe.2026.116498.

[20] Sari, H. and Sakiroglu, S., **2023**. The impact of the laser field on the electronic properties of a hydrogen molecular ion in a Gaussian quantum dot. *Physica B*, 669, p.415291. https://doi.org/10.1016/j.physb.2023.415291.

© Ariston Publications 2025. All rights reserved.

[21] Wang, W. and Xu, L. and Wei, X. and Zhang, S., **2021**. Intense-terahertz-laser modulated photoionization cross section of shallow-donor impurity in semiconductors in a magnetic field. *Results in Physics*, 20, p.103692. https://doi.org/10.1016/j.rinp.2020.103692.

[22] Pérez, L. M. and Aghoutane, N. and Laroze, D. and Díaz, P. and El-Yadri, M. and Feddi, E. M., **2023**. Intense Laser Field Effect on the Photo-Ionization Cross-Section of the First Exciton Transition in a Core/Shell Quantum Dot Submitted to an Applied Electric Field. *Coatings*, 13, p.1098. https://doi.org/10.3390/coatings13061098.

[23] Dagua-Conda, C. A. and Gil-Corrales, J. A. and Mora-Ramos, M. E. and Morales, A. L. and Duque, C. A., **2025**. Electronic Transport Properties in a One-Dimensional Sequence of Laser-Dressed Modified Pöschl-Teller Potentials. *Nanomaterials*, 15, p.1009. https://doi.org/10.3390/nano15131009.

[24] Kuo, Y. H. and Lee, Y. K. and Ge, Y. and Ren, S. and Roth, J. E. and Kamins, T. I. and Miller, D. A. B. and Harris, J. S., **2005**. Strong quantum-confined Stark effect in germanium quantum-well structures on silicon. *Nature*, 437, p.1334-1336. https://doi.org/10.1038/nature04204.

[25] Walters, G. and Wei, M. and Voznyy, O. and Quintero-Bermudez, R. and Kiani, A. and Smilgies, D. M. and Munir, R. and Amassian, A. and Hoogland, S. and Sargent, E. H., **2018**. The quantum-confined Stark effect in layered hybrid perovskites mediated by orientational polarizability of confined dipoles. *Nature Communications*, 9, p.4214. https://doi.org/10.1038/s41467-018-06746-5.

[26] Wen, G. W. and Lin, J. Y. and Jiang, H. X. and Chen, Z., **1995**. Quantum-confined Stark effects in semiconductor quantum dots. *Physical Review B*, 52, p.5913-5922. https://doi.org/10.1103/PhysRevB.52.5913.

[27] Murphy, T. and Broderick, C. A. and Peters, F. H. and O'Reilly, E. P., **2025**. Lateral Quantum-Confined Stark Effect for Integrated Quantum Dot Electroabsorption Modulators. *IEEE Journal of Selected Topics in Quantum Electronics*, 31, p.3552024. https://doi.org/10.1109/JSTQE.2025.3552024.

[28] Mojab-abpardeh, M. and Karimi, M. J., **2018**. Electron Raman scattering in a strained ZnO/MgZnO double quantum well. *Physica B*, 531, p.123-129. https://doi.org/10.1016/j.physb.2017.12.032.

[29] Betancourt-Riera, Re. and Betancourt-Riera, Ri. and Ferrer-Moreno, L. A. and Fernandez Lozada, M. and Riera, R., **2023**. Effects of an external electric field on one-phonon resonant and electron Raman scattering in a semiconductor quantum wire. *Materials Research Express*, 10, p.115005. https://doi.org/10.1088/2053-1591/ad086e.

[30] Kneipp, J. and Kneipp, K., **2024**. Surface Enhanced Nonlinear Raman Processes for Advanced Vibrational Probing. *ACS Nano*, 18, p.20851-20860. https://doi.org/10.1021/acsnano.4c07508.

[31] Tran, V. T. and Tran, T. H. and Le, M. P. and Pham, N. H. and Nguyen, V. T. and Do, D. B. and Nguyen, X. T. and Trinh, B. N. Q. and Nguyen, T. T. V. and Pham, V. T. and others, **2022**. Highly efficient photo-induced surface enhanced Raman spectroscopy from ZnO/Au nanorods. *Optical Materials*, 134, p.113069. https://doi.org/10.1016/j.optmat.2022.113069.

[32] Dakhlaoui, H. B. and Mouna, N., **2018**. Quantum size and magnesium composition effects on the optical absorption in the MgxZn1-xO/ZnO quantum well. *Chemical Physics Letters*, 693, p.40-45. https://doi.org/10.1016/j.cplett.2018.01.010.

[33] Weston, L. and Cui, X. Y. and Delley, B. and Stampfl, C., **2012**. Band offsets and polarization effects in wurtzite ZnO/Mg0.25Zn0.75O superlattices from first principles. *Physical Review B*, 86, p.205322. https://doi.org/10.1103/PhysRevB.86.205322.

[34] Zhang, H. H. and Pan, X. H. and Lu, B. and Huang, J. Y. and Ding, P. and Chen, W. and He, H. P. and Lu, J. G. and Chen, S. S. and Ye, Z. Z., **2013**. Mg composition dependent band offsets of Zn1-xMgxO/ZnO heterojunctions. *Physical Chemistry Chemical Physics*, 15, p.11231. https://doi.org/10.1039/C3CP51156A.

 © Ariston Publications 2025. All rights reserved.

[35] Tiutiunnyk, A. and Mora-Ramos, M. E. and Morales, A. L. and Duque, C. M. and Restrepo, R. L. and Ungan, F. and Martínez-Orozco, J. C. and Kasapoglu, E. and Duque, C. A., **2017**. Electron Raman scattering in a double quantum well tuned by an external nonresonant intense laser field. *Optical Materials*, 64, p.496-501. https://doi.org/10.1016/j.optmat.2017.01.001.

[36] Gil-Corrales, J. A. and Morales, A. L. and Duque, C. A., **2023**. Self-Consistent Study of GaAs/AlGaAs Quantum Wells with Modulated Doping. *Nanomaterials*, 13, p.913. https://doi.org/10.3390/nano13050913.

[37] Coleman, V. A. and Buda, M. and Tan, H. H. and Jagadish, C. and Phillips, M. R. and Koike, K. and Sasa, S. and Inoue, M. and Yano, M., **2006**. Observation of blue shifts in ZnO/ZnMgO multiple quantum well structures by ion-implantation induced intermixing. *Semiconductor Science and Technology*, 21, p.25-28. https://doi.org/10.1088/0268-1242/21/3/L02.

[38] Karcher, D. F. and Shchepetilnikov, A. V. and Nefyodov, Y. A. and Falson, J. and Dmitriev, I. A. and Kozuka, Y. and Maryenko, D. and Tsukazaki, A. and Dorozhkin, S. I. and Kukushkin, I. V. and others, **2016**. Observation of microwave induced resistance and photovoltage oscillations in MgZnO/ZnO heterostructures. *Physical Review B*, 93, p.041410. https://doi.org/10.1103/PhysRevB.93.041410.

[39] Sun, G. and Khurgin, J. B. and Friedman, L. and Soref, R. A., **1998**. Tunable intersubband Raman laser in GaAs/AlGaAs multiple quantum wells. *Journal of the Optical Society of America B*, 15, p.648-651. https://doi.org/10.1364/JOSAB.15.000648.

ARISTON PUBLICATIONS

© Ariston Publications 2025. All rights reserved.